Energy Conversion and Management 310 (2024) 118465

Contents lists available at ScienceDirect

Energy Conversion and Management

journal homepage: www.elsevier.com/locate/enconman

Research paper

Energy and dynamics analysis of a single plucking energy harvester for transient-motion-powered IoT applications

Xin Li [a,b,e], Xinyuan Chuai [a,b], Guobiao Hu [c], Daxing Zhang [a,b], Mingjing Cai [a,b], Congsi Wang [a,b], Yaowen Yang [d,1], Wei-Hsin Liao [e,1], Junrui Liang [f,1,*]

[a] Guangzhou Institute of Technology, Xidian University, Guangzhou, Guangdong, China
[b] School of Mechano-Electronic Engineering, Xidian University, Xian, Shaanxi, China
[c] Internet of Things Thrust, The Hong Kong University of Science and Technology (Guangzhou), Guangzhou, Guangdong, China
[d] School of Civil and Environmental Engineering, Nanyang Technological University, Singapore
[e] Department of Mechanical and Automation Engineering, The Chinese University of Hong Kong, Hong Kong, China
[f] School of Information Science and Technology, ShanghaiTech University, Shanghai, China

ARTICLE INFO

Keywords:
Mechanical energy harvesting
Transient motion
Magnetic plucking
Energy-centric co-design
Battery-free IoT

ABSTRACT

This study focuses on a piezo-magneto-elastic structure comprising an economical piezoelectric cantilever and a magnet pair. It is designed for efficient mechanical energy harvesting to power a battery-free motion-sensing IoT system through plucking motions. We conduct a thorough analysis and parametric study to elucidate the energy and dynamic intricacies during operation, specifically under a single plucking excitation. Beginning with a magnetic dipole–dipole model, we present a potential energy profile to intuitively elucidate and quantitatively assess the energy progression throughout a single plucking transient. By meticulously adjusting the setup parameters, the input potential energy can be precisely tuned, ensuring that the energy harvested from a single plucking motion meets the demand of each round of wireless communication. Diverging from previous power-centric investigations of plucking energy harvesters, in which continuous plucking motions are investigated, our approach provides a new perspective on the energy-centric design and transient dynamics of a single plucking motion. The importance of the energy-matching concept considering the subsequent energy-driven electronic modules is emphasized. This insight offers valuable design principles for the effective energy-centric co-design of cyber-electromechanically coupled self-powered IoT systems.

1. Introduction

Energy harvesting technology has emerged as a novel power solution for Internet of Things (IoT) systems via leveraging ambient energy sources such as solar, radio frequency (RF), and vibration. By replacing the chemical batteries with ambient energy harvesters, the self-powered IoT systems can become self-sustainable and maintenance-free; more importantly, they are more eco-friendly [1]. Kinetic energy exists everywhere in our ambiance with different forms such as mechanical vibrations and shocks [2–6]. Particularly, it is extensively contained in human motions (walking, running, finger tapping, heartbeat, respiration, etc.), structural vibrations (industrial machinery, buildings, vehicles, etc.), and fluid flows (wind, water, ocean current, etc.). Therefore, kinetic energy harvesting (KEH) technology has been regarded as one of the most promising power solutions for distributed IoT devices. It has gained increasing attention from academia and industry over the last two decades [7–9].

With the goal of replacing batteries, tremendous efforts have been devoted to improving the energy harvesting capability of KEH systems. Since the power densities of most ambient vibrations are relatively low and usually spread over a wide frequency range, various strategies have been developed to broaden the operation bandwidth and enhance the conversion efficiency of KEHs over the last decades. Those methodologies include utilizing adaptive structures [10,11], introducing nonlinearities [12,13], and modifying interface circuits [14–16]. In addition to the low power density and broadband issues, most ambient vibration energy in real application scenarios is distributed in an ultra-low frequency band, usually from several Hz to tens of Hz. It is difficult to design efficient linear energy harvesters with ultra-low natural frequencies. Thus, frequency up-conversion mechanisms utilizing impact [17] or plucking [18] motions have been proposed to address the frequency mismatch issue and improve the energy harvesting efficiency under ultra-low frequency excitations. As one

* Corresponding author.
E-mail address: liangjr@shanghaitech.edu.cn (J. Liang).
[1] The three authors have the same contribution to this study.

https://doi.org/10.1016/j.enconman.2024.118465
Received 5 January 2024; Received in revised form 3 April 2024; Accepted 22 April 2024
Available online 30 April 2024

of the earliest studies on this topic, Umeda et al. [19] proposed an impact energy harvester by using a piezoelectric unimorph disc and a steel ball falling from a specific height. When the ball bounces back off the disc, the disc vibrates at its resonant frequency, such that the bonded piezoelectric transducer generates electricity. Priya et al. [20,21] presented a windmill consisting of bimorph transducers and plectrums arranged along the circumference for harnessing energy from the wind. Pozzi et al. [22,23] proposed a wearable energy harvester for harnessing energy from a human being's knee motion. The low-frequency rotation of the knee joint was converted into the high-frequency vibration of a piezoelectric beam through a plucking mechanism. Fan et al. [24,25] designed a series of plucking harvesters that could collect kinetic energy from different spatial directions. The plucking excitations were carried out by magnetic coupling between a ferromagnetic ball and piezoelectric beams. Fu et al. [26] increased the power of a plucking energy harvester by about 150%–200% by integrating it with a synchronized switch harvesting on inductor (SSHI) interface circuit [27].

Almost all of the aforementioned studies on plucking energy harvesters are *power-centric*. Continuous plucking processes were investigated in these studies [20–26,28]. Harvested power was taken as the figure of merit evaluating the performance, nothing different from that evaluating a conventional generator. Nevertheless, merely high instantaneous power cannot guarantee the successful operation of an IoT device's sensing, computing, or transmitting task; on the other hand, accumulated energy can [29]. Therefore, different from these early studies, this study emphasizes the *energy-centric* feature of a motion-powered IoT node, i.e., considering the energy input and output of a single plucking motion, to meet the application requirement of energy-driven computing and IoT systems [29,30]. The analysis is based on a transient-motion-powered IoT system called ViPSN-pluck [31].[2] It is composed of a low-cost piezoelectric cantilever and a pair of magnets. A plucking mechanism is implemented to realize efficient energy harvesting in response to a transient excitation. Different from the previous studies of plucking energy harvesters, which considered the harvesting performance under continuous plucking motions, ViPSN-pluck carries out some deterministic IoT functions, such as sensing and wireless communication, by using the finite energy harvested from a single plucking motion. In some applications, the energy generation process is coherent with the information acquisition demand; therefore, a cyber-electromechanical co-design can be realized by taking energy-centric design thinking. Therefore, a comprehensive energy and dynamics analysis of a single plucking motion is beneficial for the holistic design of motion-powered IoT through the balance of transient energy supply and motion-coherent information demand.

2. Principle

2.1. Mechanical configuration

Fig. 1 shows a prototype of the transient plucking energy harvester and two of its applications in motion-direction detection. One driven magnet M1 is installed at the free end of the piezoelectric beam. Another driving magnet M2 is mounted on a moving frame. The poles of the two magnets are arranged to produce a repelling force between them. When the moving frame passes the piezoelectric beam, the driving magnet forces the piezoelectric beam to deform. The bent beam is released when the driving magnet M2 crosses over a critical position, where the magnetic force applied on the magnet M1 can no longer balance the restoring force of the cantilevered beam. After being released, the piezoelectric beam starts an under-damped vibration at its resonant frequency until the kinetic energy is damped out. In this transient vibration process, a part of the kinetic energy is converted into electrical energy.

[2] "ViPSN" is originally the acronym of a development platform of vibration-powered sensor nodes proposed in [29], while "pluck" stands for one of its derivatives using a plucking-motion piezoelectric energy harvester [31].

2.2. Potential energy

For the magnetic plucking harvester, its total mechanical potential energy U is the sum of the elastic energy U_e of the cantilevered beam and the magnetic potential energy U_m of the repelling magnetic pair [32], which is formulated as follows

$$U(w,b) = U_e(w) + U_m(w,b). \tag{1}$$

U is considered as a function of two key geometric parameters w (tip deflection of the cantilevered beam, i.e., transverse distance between the beam fixed end and the center of the driven magnet M1) and b (transverse distance between the beam fixed end and the center of the driving magnet M2) in the mechanical configuration, as shown in Fig. 1(b). The elastic potential energy of the cantilevered beam can be expressed as follows

$$U_e(w) = \frac{1}{2}Kw^2, \tag{2}$$

where K is the equivalent stiffness of the cantilevered beam. Based on the dipole–dipole model [33], the potential energy of the driven magnet M1 in the magnetic field generated by the driving magnet M2 can be formulated as follows

$$U_m(w,b) = -\frac{\mu_0}{4\pi}\left(\nabla\frac{\mathbf{m}_{O_2}\cdot\mathbf{r}_{O_2O_1}}{\|\mathbf{r}_{O_2O_1}\|_2^3}\right)\cdot\mathbf{m}_{O_1}, \tag{3}$$

where μ_0 is the vacuum permeability; $\mathbf{r}_{O_2O_1}$ denotes the distance vector from the center of driving magnet M2 to the center of driven magnet M1; $\mathbf{m}_{O_1}$ and $\mathbf{m}_{O_2}$ represent the magnetic moment vectors of the M1 and M2, respectively. For permanent magnets, their magnetic moment vectors can be written as follows

$$\mathbf{m}_{O_1} = \begin{bmatrix} \frac{B_r}{\mu_0}V_{O_1} \\ 0 \end{bmatrix}, \quad \mathbf{m}_{O_2} = \begin{bmatrix} \frac{B_r}{\mu_0}V_{O_2} \\ 0 \end{bmatrix}, \tag{4}$$

where B_r is the magnets residual flux density; B_r/μ_0 represents the magnitude of the magnetization vector; and V_{O_1} and V_{O_2} are the volumes of the two magnets M1 and M2, respectively. Substituting the above vectors into (3) yields the potential energy in the scalar form as follows

$$U_m(w,b) = -\frac{\mu_0 m_{O_1} m_{O_2}}{4\pi}\left(r_{O_2O_1}^{-3} - 3d^2 r_{O_2O_1}^{-5}\right), \tag{5}$$

where m_{O_1} and m_{O_2} are the square norms of $\mathbf{m}_{O_1}$ and $\mathbf{m}_{O_2}$; $r_{O_2O_1}$ is the square norm of $\mathbf{r}_{O_2O_1}$, i.e., the distance between the center of the driving magnet M2 and that of the driven magnet M1; b and d are the transverse and longitudinal distances between the centers of the two magnets, respectively. Under the small deflection assumption of beams, the angle α of the driven magnet M1 at the cantilever tip approximately equals that of the cantilevered beam, i.e., $\alpha \approx \sin^{-1}(w/L)$, where L is the length of the piezoelectric beam. Therefore, d and $r_{O_2O_1}$ can be respectively formulated as follows

$$d = d_0 + L(1-\cos\alpha), \tag{6}$$

$$r_{O_2O_1} = \sqrt{(w-b)^2 + d^2}, \tag{7}$$

where d_0 is the initial longitudinal distance between the two magnets.

2.3. Dynamic model

The transverse magnetic force is formulated as the negative derivative of the magnetic potential energy with respect to the transverse distance w, i.e.,

$$\begin{aligned} F_m(w,b) &= -\frac{\mathrm{d}U_m(w,b)}{\mathrm{d}w} \\ &= \frac{3\mu_0 m_{O_1} m_{O_2}(w-b)}{4\pi r_{O_2O_1}^5 L}\left\{\frac{dw}{w-b} - \sqrt{L^2-w^2}\right. \\ &\quad \left. -\frac{5d}{r_{O_1O_2}^2}\left[w(w-b) - d\sqrt{L^2-w^2}\right]\right\}. \end{aligned} \tag{8}$$

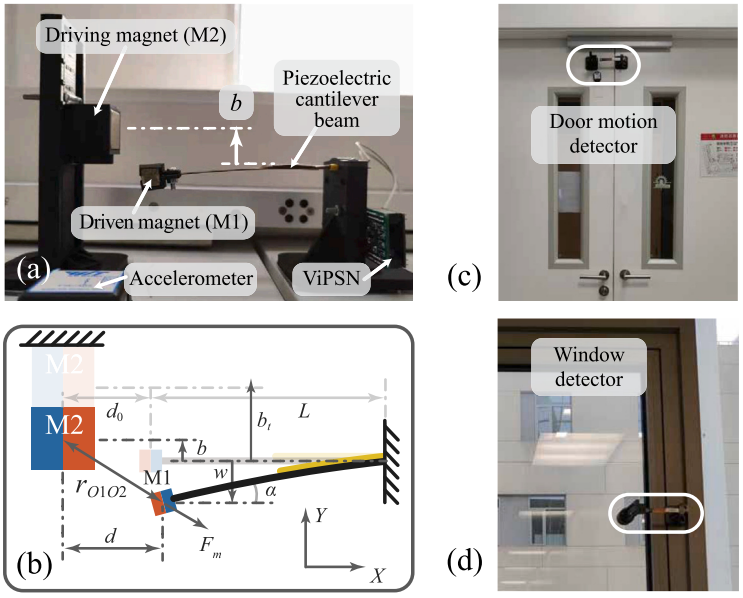

Fig. 1. Piezo-magneto-elastic plucking harvester with application examples. (a) The full setup of ViPSN-pluck. (b) Mechanical configuration. (c) Application as a door motion detector. (d) Application as a window motion detector.

Table 1
Parameters of the prototyped plucking energy harvester.

Symbol	Description	Value
M	Equivalent mass of cantilevered beam with tip magnet M1	11.7 g
D	Equivalent damping coefficient	0.0246 N s/m
K	Equivalent bending stiffness	173.6968 N/m
C_p	Piezoelectric clamped capacitance	37.8412 nF
ψ_e	Electromechanical coefficient	0.13901 mN/V
L	Length of cantilevered beam	105 mm
d_0	Initial longitudinal interval of the driving and driven magnets	28 mm
V_{O1}	Volume of driven magnet M1	$10\times10\times10$ mm^3
V_{O2}	Volume of driving magnet M2	$20\times20\times20$ mm^3
B_r	Residual flux density of magnets	1.2 T
μ_0	Magnetic constant	$4\pi\times10^{-7}$ H/m

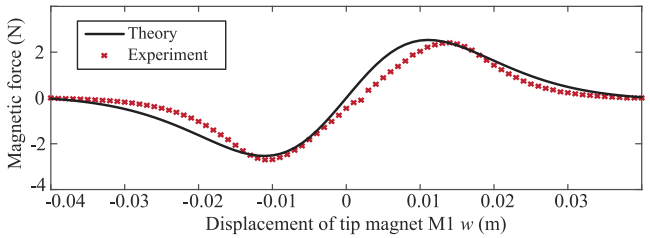

Fig. 2. Theoretical and experimental results of magnetic force $F_m(w,b)$ $(b=0)$.

According to (8) and with the related parameters of the prototyped plucking energy harvester in this study, which are listed in Table 1, we can draw the theoretical magnetic force picture, as shown by the black solid line in Fig. 2. The measured force shows a good agreement with the theoretical one; therefore, the dipole–dipole model is validated. As shown by Fig. 2, the magnetic force has the same sign as the M1 displacement; therefore, it is a repelling force, which effectively acts as a nonlinear and negative stiffness. Those parameters listed in Table 1 are also used in the simulation study and experimental validation in Sections 4 and 5, respectively.

Given the balance of forces in the mechanical domain and Kirchhoff's current law (KCL) in the electrical domain, the piezo-magneto-elastic coupled system can be formulated with a lumped single-degree-of-freedom (SDOF) model. The governing equations are shown as follows

$$\begin{cases} M\ddot{w} + D\dot{w} + Kw + \psi_e v_p + F_m(w,b) = 0, \\ i_p = \psi_e \dot{w} - C_p \dot{v}_p, \\ v_p = i_p R_l, \end{cases} \tag{9}$$

where M is the equivalent mass of the piezoelectric beam with a tip mass M1; D is the equivalent damping coefficient; ψ_e is the electromechanical coupling coefficient; v_p represents the piezoelectric output voltage; i_p is the current flowing through the load; and C_p is the clamped capacitance of the piezoelectric transducer; R_l is the equivalent load resistance.

Eq. (9) describes how the transverse distance w of the piezo-magneto-elastic system proceeds along with the time variation. Because $F_m(w,b)$ the magnetic force formulated in (8) is a nonlinear function of w, the closed-form solution of (9) is uneasy to derive. Numerical simulations are performed using the Runge–Kutta solver in Matlab to investigate the dynamics of the system in the plucking process. The simulation results will be discussed in Section 4.

3. Energy analysis

A single plucking process can be broken down into two successive phases, the *potential energy pre-charging* and *under-damped vibration after release* phases. The two phases are separated by a *critical position* at which the cantilevered beam is released, say, the firing point of plucking action. Fig. 3 illustrates the contours of total potential energy $U(w,b)$ and the potential pictures under different driving magnet M2 positions b. Fig. 4 further shows the profile in a 3D plot to give an intuitive idea about the ridge and trough, which form the complex energy picture of a plucking process.

3.1. Potential energy pre-charging (PEP) phase

In the potential energy pre-charging stage, as the driving magnet M2 approaches the driven magnet M1, i.e., the distance b approaches a slightly positive value from the negative side, or a slightly negative

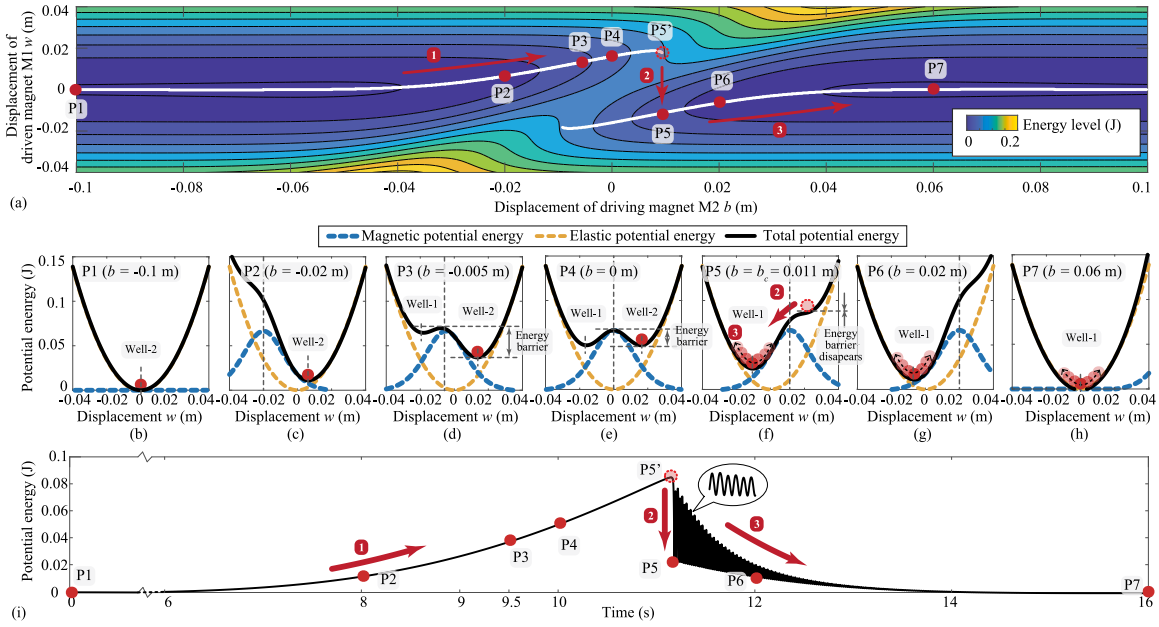

Fig. 3. Energy diagrams showing the potential energy profile in a single plucking motion. (a) Contours of total potential energy. (b)–(h) The variation of potential wells along the moving way of M2. (b) Starting position with a single linear well. (c) and (d) Intermediate positions with two asymmetric wells. (e) Intermediate position with two symmetric wells. (f) Critical position at which the energy barrier disappears and the beam starts to oscillate. (g) and (h) Oscillations at different (nonlinear or linear) monostable wells. (i) Time-displacement history of potential energy.

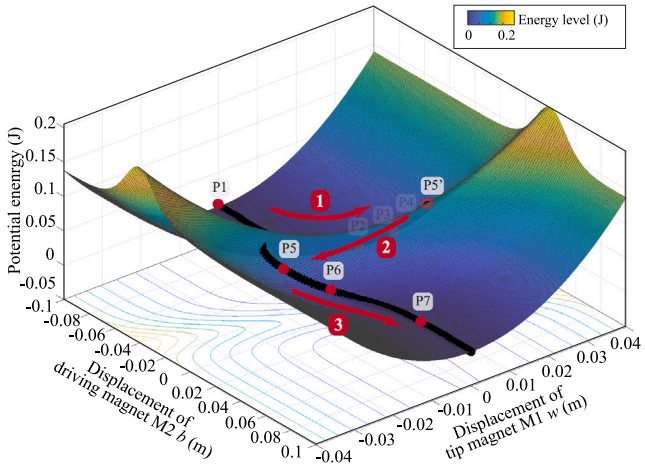

Fig. 4. Profile of total potential energy $U(w, b)$ of a plucking structure.

value from the positive side. Compared with the relative high-speed free vibration after the plucking release, the potential energy pre-charge stage can be regarded as a quasi-static procedure, in which the piezoelectric beam is pushed away from its initial equilibrium position by the repelling magnetic force. This stage ends when the magnetic force reaches the maximum and cannot balance the restoring force of the piezoelectric beam anymore, along the proceeding way of the driving magnet M2.

The physical principle of this quasi-static process can be better explained with the potential energy profiles shown in Figs. 3 and 4. This pre-charging phase proceeds following the path from the P1 position to the P5' position. According to the characteristics of the potential energy profile shown in Fig. 3(a), a PEP phase can be further broken down into two sub-phases.

3.1.1. *Initial monostable sub-phase*

The representative positions in this phase are P1 and P2. In this phase, the plucking harvester is a monostable system, since there is only one stable equilibrium position in the potential picture, as shown by the black solid line in Fig. 3(b) and (c). The red ball in the figure represents the transverse position of the driven magnet M1. As the total potential energy is the sum of the linear elastic one (parabolic yellow dashed line) and the nonlinear magnetic one (bell-shaped blue dashed line), the black line distorts as b the distance between the center lines of the two dashed lines changes. As demonstrated in Fig. 3(b), when the driving magnet M2 is at position P1, the total potential energy is at its lowest point. As b increases and attains position P2, the potential well-2 is lifted up as shown in Fig. 3(c). As the driving magnet M2 keeps moving, the potential well-2 continues to be elevated. In the meanwhile, after some positions, another potential well-1 is formed, such that the system enters the bistable sub-phase.

3.1.2. *Bistable phase sub-phase*

The representative positions in the bistable phase are P3 and P4, whose potential energy wells are illustrated in 3(d) and (e). The two potential wells are asymmetric at their first appearance, as shown in 3(d). When $b = 0$, their shapes become symmetric, as shown in 3(e). As the driving magnet M2 further moves to the positive range, i.e., $b > 0$, the double-well potential picture becomes asymmetric again. But in this asymmetric case, the potential well-2 is squeezed and becomes narrower and shallower, while the potential well-1 becomes wider and deeper.

3.2. *Critical position*

As b further proceeds, the plucking harvester transits from bistable to monostable at a critical position b_c. The potential picture at the critical position is illustrated in Fig. 3(f). This critical instant is also illustrated by the arrows from P5' to P5 in Fig. 3(a) and (i) and Fig. 4.

The bistable to monostable transition can be explained by the bifurcation theory [34]. Fig. 5(a) and (b) show the bifurcation diagram of the equilibrium solutions and the transition paths of the plucking harvester when the driving magnet M2 moves in either forward or

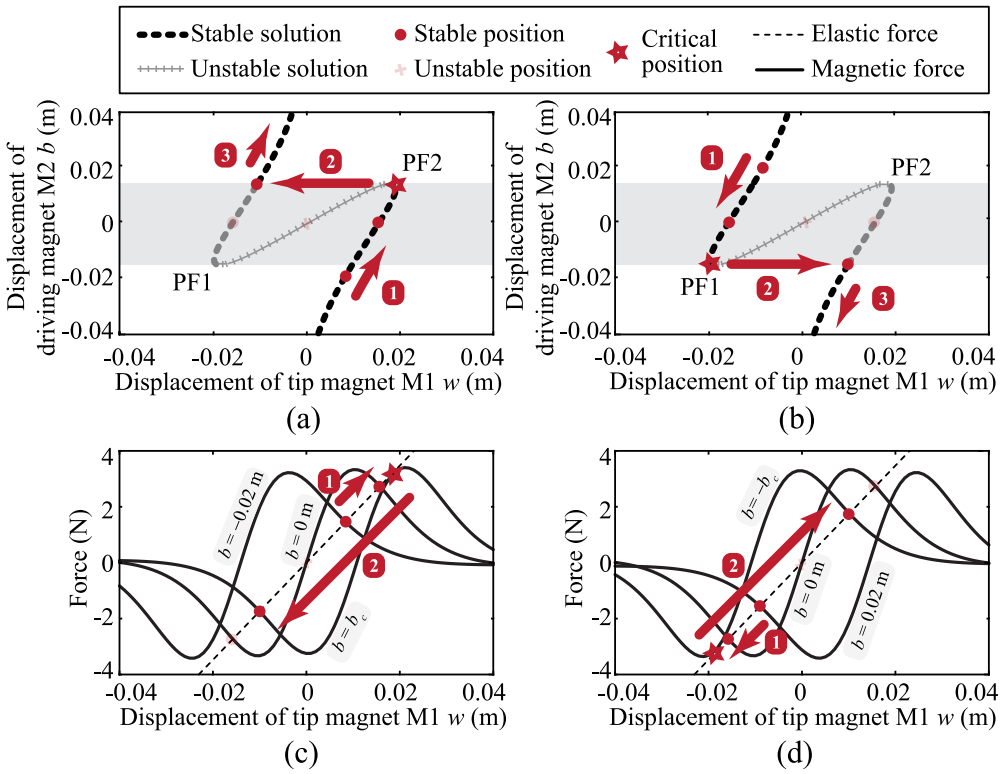

Fig. 5. Moving equilibrium positions and critical positions. (a) and (b) The moving equilibrium positions of the magnetic and elastic forces in forward and reverse driving directions, respectively. (c) and (d) Magnetic and elastic forces over beam deflection w under different driving magnet positions b, respectively.

reverse directions. The equilibrium points can be found as the crossover points of the negative elastic force $F_e = Kw$ and the magnetic force $F_m(w, b)$ formulated in (8). The two forces are illustrated in straight dashed lines and s-shape solid lines in Fig. 5(c) and (d), respectively. The s-shape magnetic force curve can move back and forth along the horizontal axis as the driving magnet position b moves. When b is either very small or very large, there is only one crossover point, i.e., the equilibrium point of a potential well. When $-b_c < b < b_c$, there are three crossover points, which represent two stable solutions and one unstable solution. Although another stable solution is formed, the system still proceeds around the original stable solution branch. When $b = \pm b_c$, the linear line is in tangent to an s-shape line case at either its upper or lower u-turn segments. As we can observe in Fig. 5(a), the stable trough line and unstable ridge line merge at the critical point, which is marked with a star. After this point, if b continues to proceed beyond b_c, the original equilibrium solution branch must be suddenly broken up at the bifurcation point PF2, such that the system is forced to jump to another potential trough branch. Along with this equilibrium jump from P5' to P5, a specific amount of potential energy is released.

3.3. Under-damped vibration after release (UVR) phase

When the driving magnet M2 moves to position P5, the potential well-2 disappears, as shown in Fig. 3(g) to (h). As the system always tends to stabilize at the bottom of a potential well, the red ball will fall to the bottom of well-1 from the just disappeared well-2. Given the energy drop from the higher well-2 at P5' point to the lower well-1 at P5 point around the critical position, the released energy excites the cantilevered beam to an under-damped vibration until the released energy is damped out. During the under-damped vibration, a part of the kinetic energy is converted into electricity by the piezoelectric transducer.

Considering the continuous movement of the driving magnet M2 from point P1 to P7, the time history of the potential energy in the plucking process is illustrated in Fig. 3(i). The PEP phase, critical instant, and UVR phase are illustrated as processes 1 to 3, respectively, with red arrows in all the sub-figures of Figs. 3 and 4. The mutual relations among these figures can be figured out by referring to the corresponding processes with the same numbers.

3.4. Energy tuning

Two geometric tuning mechanisms can be taken for adjusting the harvested energy. They might bring much convenience for the customization of a plucking harvester. In particular, when such a transient-motion-powered plucking harvester is used to energize some energy-driven devices [30], such as ViPSN-pluck [31].

3.4.1. Input energy tuning in the PEP phase

During the plucking motion, the energy is input in mechanical form. The amount of input energy can be adjusted by tuning d_0, i.e., the longitudinal distance between the driving and driven magnets. In the PEP phase, as shown from Fig. 3(b) to (f), the potential energy rises from zero at the P1 point to the height of the critical point P5. Such an energy difference is the input potential energy. Given the same mechanical setup, the critical position of the plucking harvester is adjustable by tuning the longitudinal distance between the two magnets, i.e., d_0. The effect of shortening d_0 is to increase the height of the potential barrier under the symmetric bistable case. As shown in Fig. 6(a), a smaller d_0 yields a higher barrier in the middle of the potential curve. In the previous studies of periodic plucking structures, the effect of the moving magnet-introduced energy barrier was modeled as a symmetric pulsed force excitation [35,36]. Such a solution is not applicable for the analysis of a single plucking motion. In this study, by using the explanation of varying potential well, the input energy can be evaluated by intuitively observing the height differences at the critical plucking position b_c. As shown in Fig. 6(b), decreasing d_0 leads to a larger potential energy drop at the corresponding critical position.

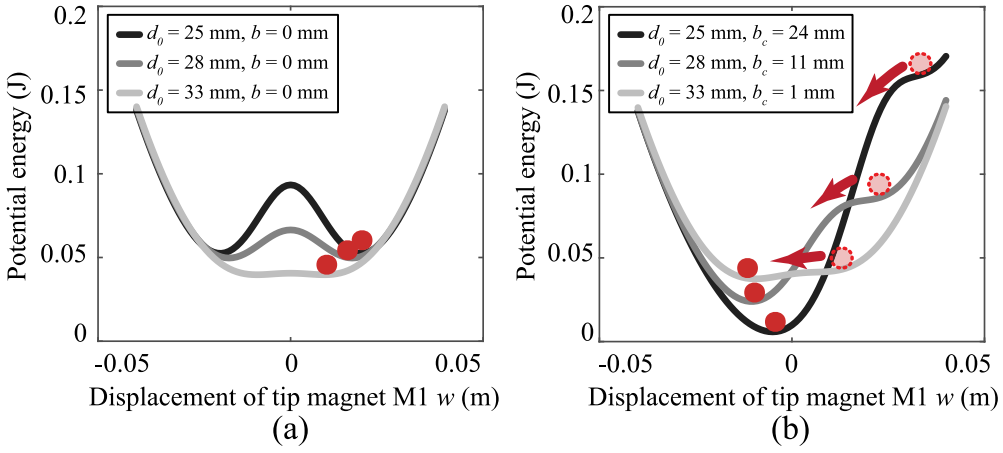

Fig. 6. Input potential energy under different longitudinal distances d_0. (a) In the symmetric positions ($b = 0$). (b) In the critical positions ($b = b_c$).

In the design of an energy-driven application, d_0 must be carefully adjusted below a specific value to give sufficient energy for satisfying the demand of some pre-defined IoT functions. It should be also noted that a smaller d_0 indicates the requirement of a larger driving force to move magnet M2 for carrying out a plucking motion. Hence, a compromise should be made to select a suitable distance d_0 for simultaneously satisfying the IoT demand and driving comfort. Some experimental results of the harvested energy under different d_0 setups are also provided in Section 5.3.

3.4.2. Released energy tuning in UVR phase

After the PEP phase, the input mechanical energy is stored in the bent beam in the form of strain energy. On the other hand, not all the input energy must be released to drive the cantilevered beam vibration. If we tune the stop position of the driving magnet M2, i.e., b_t as shown in Fig. 1(b), the amount of released energy can also be adjusted. The idea can be intuitively understood by comparing Fig. 3(f) to (h). If the stop position of the driving magnet M2 is set at the critical point P5, the depth of the final potential well-1 is shallower, compared with the case stopping at P6; therefore, the released energy is less. The same conclusion can be drawn by comparing the cases when M2 stops at P6 and P7. Since the vibration after being released involves some complex transient interactions between the elastic, piezoelectric, and magnetic parts, which cannot be formulated analytically, the effect of released energy tuning can be studied based on the numerical simulation and experimental results presented in Sections 4 and 5, respectively.

4. Dynamics simulation

To obtain more understanding on the plucking dynamics of the piezo-magneto-elastic structure, simulation is performed based on the model formulated in the Eqs. (8) and (9). The equations are solved in Matlab using the Runge–Kutta numerical method. Since a weakly coupled piezoelectric beam is used in this study, the electrical to mechanical backward coupling has little effect on the system dynamics; therefore, in the simulation, the open-circuit condition is considered for the electrical part, i.e., using a $R_l = \infty$; therefore, $i_p = 0$.

Fig. 7 shows the dynamic response of the plucking harvester by showing its time-displacement history and phase portrait. The driving magnet M2 moves at a speed of 1 m/s in the simulation. To validate the dynamic model under different parametric cases, the stop position of M2, i.e., b_t, is set to different values corresponding to the positions of P4, P5, P6, and P7, whose potential pictures are illustrated in Fig. 3(e)–(h), respectively. Setting different b_t values also helps evaluate the dynamic effect after taking the released energy tuning design, which was explained in Section 3.4. The other parameters used in the simulation follow those listed in Table 1.

From all sub-figures in Fig. 7, we can observe that the driven magnet M1 departs from the initial equilibrium $w = 0$ position, then it is dragged to a position, where w attains its maximum value. After that, the cantilevered harvester goes through an under-damped vibration until it rests at the bottom of a potential well. The critical condition $b_t = b_c$ sets a boundary differentiating whether the plucking action can be successfully carried out or not. For those $b_t < b_c$ cases, e.g., that described in Fig. 3(a) and (b), the vibration magnitude after release is much smaller than the other $b_t \geq b_c$ cases. The displacement is always in the same polarity, i.e., never crosses the $w = 0$ line in these cases; therefore, the plucking action cannot be successfully triggered. The driven magnet is eventually trapped in the same potential well. For those $b_t \geq b_c$ cases, which are described in Fig. 3(c)–(h), w crosses zero after successful plucking actions. The larger b_t, the closer it approaches the linear under-damped vibration with an initial deflection, in which it records a maximum vibration magnitude because all the input energy is released for vibration. As we can observe from these figures, the potential well, at which the vibrator finally rests, is well-1, whose position is at some negative w values.

These results not only validate the theoretical model, which can be used for elaborating the plucking dynamics but also validate the above-mentioned released energy tuning capability through the stop position design of the driving magnet M2. The tailorable harvested energy of the plucking harvester is a unique mechanical feature for guaranteeing the robust performance of an energy-driven IoT system [30]. In contrast, in other IoT designs based on the continuous power input and immediate mechanical-to-electrical power conversions, such as solar, RF, thermoelectric, or continuous vibration, the energy-level monitoring and under-voltage lockdown functions must be carried out by extra power management circuits [29], which increase the complexity of the cyber-electromechanically integrated solution. Moreover, such a feature of tailorable input energy has been further explored for making a self-powered sensor-free motion-direction detector in the authors' ViPSN-pluck design [31].

5. Experimental investigation

5.1. ViPSN-pluck prototype

Experiments evaluating the dynamic behaviors under different parametric conditions of the plucking energy harvester are carried out based on the ViPSN-pluck IoT system, which was developed by the authors' research group [31]. The original study emphasizes the holistic energy-driven IoT design and cyber-electromechanical synergy, while this study emphasizes a more in-depth study of its mechanical part through energy and dynamics analyses.

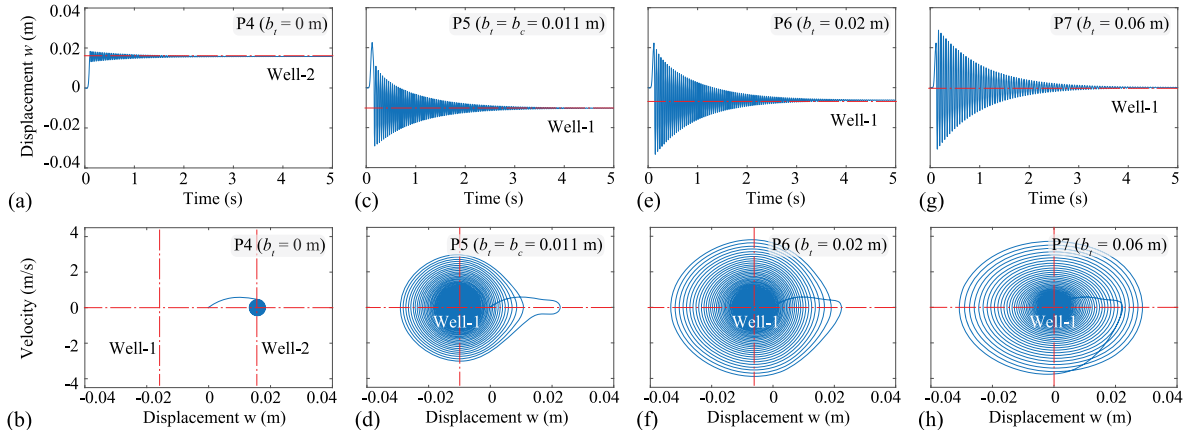

Fig. 7. Simulation results of time-displacement history and phase portrait under different b_t the stop positions of driving magnet M2. (a) and (b) M2 stops at the P4 position, before the critical position P5. (c) and (d) M2 stops at the critical position P5. (e) and (f) M2 stops at position P6. (g) and (h) M2 stops at position P7.

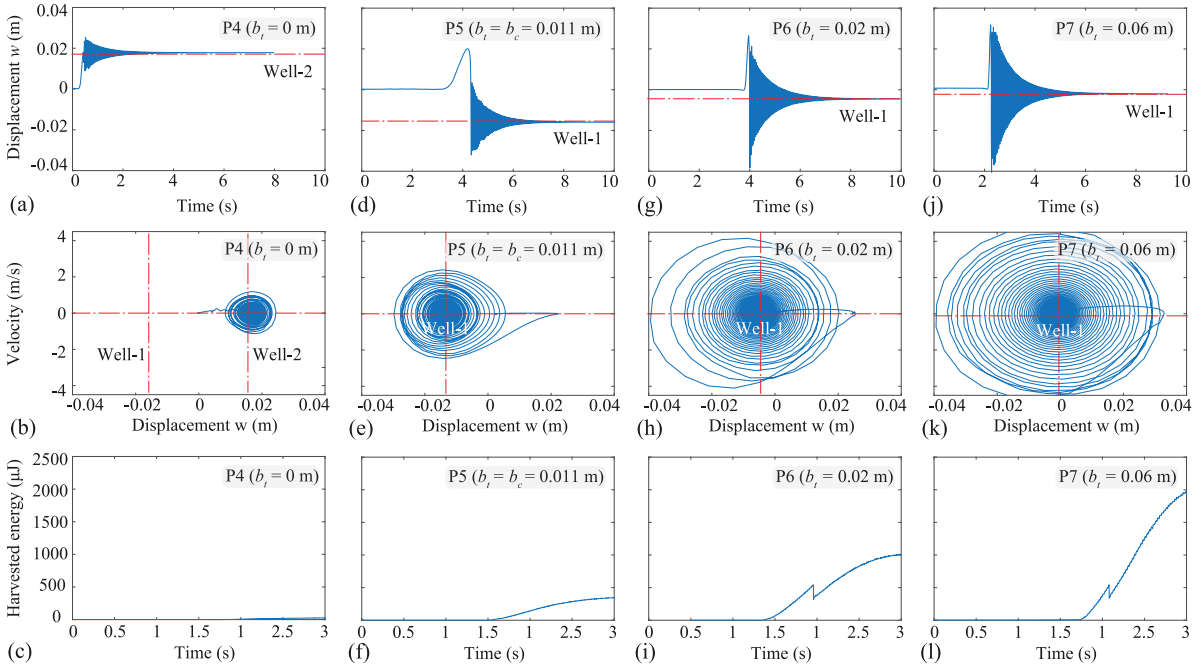

Fig. 8. Experimental results of time-displacement history, phase portrait, and harvested energy under different b_t. (a)–(c) M2 stops at the P4 position, before the critical position P5. (d)–(f) M2 stops at the critical position P5. (g)–(i) M2 stops at position P6. (j)–(l) M2 stops at position P7.

The full setup of the motion-powered transmitter in ViPSN-pluck was shown in Fig. 1(a). The parameters of this prototyped plucking harvester were listed in Table 1. In the setup, a driving magnet M2 is fixed at a 3D-printed holder, which is installed on a moving object, e.g., an entrance door. A piezoelectric beam with a driven magnet M1 on its tip is clamped at another holder installed on a fixed object, e.g., the door frame. The moving acceleration and speed of M2 are measured by a wireless accelerometer (WT901BLECL, WIT motion Co.) mounted on the moving object. The velocity and displacement of the plucking beam are measured by a laser Doppler vibrometer (OFV-552/5000, Polytec GmbH).

The small block in the bottom right of Fig. 1(a) is a ViPSN evaluation board. ViPSN is an open-sourced development platform, which was also proposed by the authors' research group [29].[3] It provides a well-rounded solution that includes a small vibrator, energy enhancement, energy management, Bluetooth low energy (BLE) embedded system, and a mobile app for demonstration, supporting the general-purpose research and development of vibration-powered IoT systems. ViPSN can be easily extended or reprogrammed to meet the implementation demand of some new ideas for motion-powered things [37–40], e.g., the ViPSN-pluck design [31].

5.2. Measurement results

Experiments are carried out to validate the simulation results shown in Fig. 7. Fig. 8 shows the corresponding measurement results of a prototyped ViPSN-pluck harvester by changing b_t the stop position of the driving magnet M2. Similar to the layout of Fig. 7, in Fig. 8, the first row shows the time-displacement history; the second row shows the phase portrait. By comparing the sub-figures in these first two rows of the two figures, we can see that the experimental results show a good agreement with the simulation ones, in terms of curve outline, time and magnitude scales, etc.

Fig. 8 has an extra third row showing the harvested energy in the four cases, in which the transformed energy is rectified into dc form by

[3] https://github.com/METAL-ShanghaiTech/ViPSN

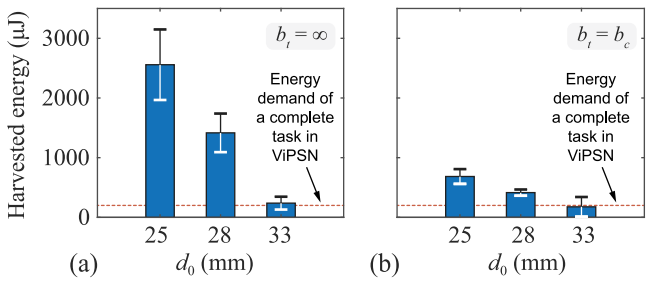

Fig. 9. Harvested energy after a single plucking motion under different d_0 the longitudinal distance between two magnets. (a) $b_t = \infty$ case, in which M2 stops far away from the plucking harvester. (b) $b_t = b_c$ case, in which M2 stops at the critical plucking position.

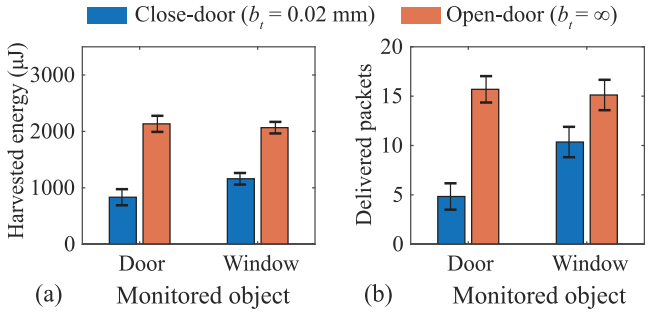

Fig. 10. The ViPSN-pluck that consists of the proposed plucking harvester and the IoT system - ViPSN is installed on a door and a window for open/close motion detection. (a) Measured energies that are collected in the storage capacitor of the ViPSN-pluck during the open/close-door/window processes. (b) Number of BLE beacon packets sent out by ViPSN-pluck during the open/close-door/window processes.

using a bridge rectifier. From the final harvested energy result, we can see that the unsuccessful plucking motion, where $b_t < b_c$, gives almost zero energy output. Comparing those successful plucking cases, where $b_t \geq b_c$, more energy can be harvested if the driving magnet M2 stops at a larger b_t position.

In general, the theoretical model, varying potential well analysis, and energy tuning methods introduced in the above Sections are validated by experiments based on the ViPSN-pluck prototype.

5.3. Robustness of self-powered operation

The most important issue of a self-powered system is whether the harvested energy is sufficient to power a complete IoT task. For example, according to our previous study [41,42], ViPSN requires 201.54 μJ energy to perform a complete task, which includes system initialization, sensing, and Bluetooth low energy (BLE) wireless transmission. To better evaluate the operational robustness of this self-powered design, we record the amounts of harvested energy in a single plucking motion under two b_t and three d_0 conditions. Fig. 9 shows the statistical average levels of the harvested energy in the six cases. Error bars are added to indicate the variation interval after repeated tests. It can be seen that with the increase of d_0, the harvested energy monotonically decreases. To ensure the harvested energy is sufficient for powering the execution of a complete IoT task, we should have a small d_0, where the lowest harvested energy is above the specific energy demand of 201.54 μJ. According to Fig. 9, such a design target is achievable when d_0 is set to 25 mm or 28 mm.

Several field tests in real scenarios are conducted, as shown in Video S1. The plucking harvester prototype, together with the IoT node - ViPSN, is installed on a door and a window, as shown in Fig. 1(c) and (d), to detect the open/close motion. Once an open/close motion occurs, the plucking harvester will trigger ViPSN. Then ViPSN will repeatedly send BLE beacon packets to the system terminal until the energy collected by the plucking harvester is consumed. In the experiment, a smartphone is used as the system terminal. Fig. 10(a) shows the measured energies that were collected in the storage capacitor of the ViPSN-pluck during the open/close-door/window processes. As stated before, the energies collected in different processes are different. The power consumption for sending a single BLE beacon packet is almost fixed and constant. Thus, by counting the number of the BLE beacon packets received by the smartphone, the motion direction can be identified. Fig. 10(b) shows the number of the delivered BLE beacon packets in the tests. It can be found that the average number of delivered packets during the open-door process is about 15, while that during the close-door process is only about 5. Similarly, more BLE beacon packets can be delivered to the smartphone in the open-window process than the close-window process. By implementing a simple code on the smartphone, it can directly tell whether an open or close motion occurs based on the number of received packets.

The unique mechanical feature of a single plucking motion offers the most important factor in the design of a robust energy-driven IoT system. On the other hand, the cyber-electromechanical synergy is of importance as well toward a practical implementation. One can refer to our previous paper introducing ViPSN-pluck for more information about the co-design methodology based on the ViPSN development platform [29,31].

6. Conclusion

The plucking structures were extensively discussed for frequency up-conversion in piezoelectric energy harvesting. Nevertheless, almost all of the previous studies were conducted based on continuous or periodic excitation scenarios and taken *power-centric thinking*, which cannot guarantee an indivisible IoT operation. In real applications, the *energy-centric thinking* is more appropriate. Therefore, the energy and dynamics analysis of a single plucking motion discussed in this paper is necessary. This paper fulfilled this task by presenting a comprehensive analysis of the energy and dynamics of a single plucking transient motion. The potential energy precharging mechanism and energy tuning capability were emphasized, because they contribute to the unique feature of a plucking energy harvester, compared to other existing designs that were driven by continuous excitation. The effects of the magnet layout were quantitatively evaluated in simulation and experiment, in terms of dynamic responses and harvested energy. The new insight obtained in this study not only enriches the fundamental knowledge of plucking structural dynamics in a single plucking scenario but also synergizes with the fields of energy harvester design and battery-free sensing applications.

CRediT authorship contribution statement

Xin Li: Writing – review & editing, Writing – original draft, Visualization, Validation, Supervision, Software, Resources, Project administration, Methodology, Investigation, Funding acquisition, Formal analysis, Data curation, Conceptualization. **Xinyuan Chuai:** Data curation, Software, Writing – review & editing. **Guobiao Hu:** Writing – review & editing, Writing – original draft. **Daxing Zhang:** Funding acquisition. **Mingjing Cai:** Investigation. **Congsi Wang:** Funding acquisition. **Yaowen Yang:** Supervision. **Wei-Hsin Liao:** Supervision. **Junrui Liang:** Supervision, Funding acquisition, Writing – review & editing.

Declaration of competing interest

We declare that there is no conflict of interest between the authors.

Data availability

Data will be made available on request.

Acknowledgments

This work was supported by the Fundamental Research Funds for the Central Universities of China under Project 01151901, the National Natural Science Foundation of China under Grants 62271319, the Natural Science Foundation of Shanghai under Grant 21ZR1442300, and the Innovation and Technology Commission, Hong Kong Special Administrative Region, China, under Project MRP/030/21.

Appendix A. Supplementary data

Supplementary material related to this article can be found online at https://doi.org/10.1016/j.enconman.2024.118465.

References

[1] Sigrist L, Stricker N, Bernath D, Beutel J, Thiele L. Thermoelectric energy harvesting from gradients in the earth surface. IEEE Trans Ind Electron 2019.
[2] Liu H, Zhong J, Lee C, Lee S-W, Lin L. A comprehensive review on piezoelectric energy harvesting technology: materials, mechanisms, and applications. Appl Phys Rev 2018;5(4):041306.
[3] Wang J, Zhao L. Toward nonlinear galloping energy harvesting interfaced with different power extraction circuits. IEEE/ASME Trans Mechatronics 2022;27(5):2678–89.
[4] Gao Y, Liang J, Liao Y. Multiple harmonics extended impedance model of piezoelectric energy harvesting systems. IEEE/ASME Trans Mechatronics 2021;27(2):1185–95.
[5] González A, Olazagoitia JL, Viñolas J, Ulacia I, Izquierdo M. An innovative energy harvesting shock absorber system for motorbikes. IEEE/ASME Trans Mechatronics 2021;27(5):3110–20.
[6] Pan Q, Wang B, Zhang L, Li Z, Yang Z. Whisk-inspired motion converter for ocean wave energy harvesting. IEEE/ASME Trans Mechatronics 2021;27(3):1808–11.
[7] Tao K, Zhao Z, Yang Y, Wu J, Li Y, Fan K, et al. Development of bipolar-charged electret rotatory power generator and application in self-powered intelligent thrust bearing. Nano Energy 2021;90:106491.
[8] Wu X, Cao W, Yu H, Zhang Z, Leng Y, Zhang M. Generating electricity during locomotion modes dominated by negative work via a knee energy-harvesting exoskeleton. IEEE/ASME Trans Mechatronics 2022;27(6):4451–61.
[9] Gao F, Liu G, Fu X, Li L, Liao W-H. Lightweight piezoelectric bending beam-based energy harvester for capturing energy from human knee motion. IEEE/ASME Trans Mechatronics 2021;27(3):1256–66.
[10] Tang Q, Li X. Two-stage wideband energy harvester driven by multimode coupled vibration. IEEE/ASME Trans Mechatronics 2014;20(1):115–21.
[11] Hu G, Liang J, Lan C, Tang L. A twist piezoelectric beam for multi-directional energy harvesting. Smart Mater Struct 2020;29(11):11LT01.
[12] Khameneifar F, Arzanpour S, Moallem M. A piezoelectric energy harvester for rotary motion applications: Design and experiments. IEEE/ASME Trans Mechatronics 2012;18(5):1527–34.
[13] Lu Z, Brennan MJ, Yang T, Li X, Liu Z. An investigation of a two-stage nonlinear vibration isolation system. J Sound Vib 2013;332(6):1456–64.
[14] Lefeuvre E, Badel A, Richard C, Guyomar D. Piezoelectric energy harvesting device optimization by synchronous electric charge extraction. J Intell Mater Syst Struct 2005;16(10):865–76.
[15] Liang J, Liao W-H. Impedance modeling and analysis for piezoelectric energy harvesting systems. IEEE/ASME Trans Mechatronics 2012;17(6):1145–57.
[16] Zhao L, Tang L, Liang J, Yang Y. Synergy of wind energy harvesting and synchronized switch harvesting interface circuit. IEEE/ASME Trans Mechatronics 2016;22(2):1093–103.
[17] Ylli K, Hoffmann D, Willmann A, Becker P, Folkmer B, Manoli Y. Energy harvesting from human motion: exploiting swing and shock excitations. Smart Mater Struct 2015;24(2):025029.
[18] Pillatsch P, Yeatman E, Holmes A. A scalable piezoelectric impulse-excited energy harvester for human body excitation. Smart Mater Struct 2012;21(11):115018.
[19] Umeda M, Nakamura K, Ueha S. Analysis of the transformation of mechanical impact energy to electric energy using piezoelectric vibrator. Japan J Appl Phys 1996;35(5S):3267.
[20] Priya S, Chen C-T, Fye D, Zahnd J. Piezoelectric windmill: A novel solution to remote sensing. Japan J Appl Phys 2004;44(1L):L104.
[21] Priya S. Modeling of electric energy harvesting using piezoelectric windmill. Appl Phys Lett 2005;87(18):184101.
[22] Pozzi M, Zhu M. Plucked piezoelectric bimorphs for knee-joint energy harvesting: modelling and experimental validation. Smart Mater Struct 2011;20(5):055007.
[23] Pozzi M, Aung MS, Zhu M, Jones RK, Goulermas JY. The pizzicato knee-joint energy harvester: characterization with biomechanical data and the effect of backpack load. Smart Mater Struct 2012;21(7):075023.
[24] Fan K, Chang J, Chao F, Pedrycz W. Design and development of a multipurpose piezoelectric energy harvester. Energy Convers Manag 2015;96:430–9.
[25] Fan K, Chang J, Pedrycz W, Liu Z, Zhu Y. A nonlinear piezoelectric energy harvester for various mechanical motions. Appl Phys Lett 2015;106(22):223902.
[26] Fu H, Yeatman EM. Effective piezoelectric energy harvesting using beam plucking and a synchronized switch harvesting circuit. Smart Mater Struct 2018;27(8):084003.
[27] Guyomar D, Badel A, Lefeuvre E, Richard C. Toward energy harvesting using active materials and conversion improvement by nonlinear processing. IEEE Trans Ultrason Ferroelectr Freq Control 2005;52(4):584–95.
[28] Dauksevicius R, Kleiva A, Grigaliunas V. Analysis of magnetic plucking dynamics in a frequency up-converting piezoelectric energy harvester. Smart Mater Struct 2018;27(8):085016.
[29] Li X, Teng L, Tang H, Chen J, Wang H, Liu Y, et al. ViPSN: A vibration-powered IoT platform. IEEE Internet Things J 2020;8(3):1728–39.
[30] Sliper ST, Cetinkaya O, Weddell AS, Al-Hashimi B, Merrett GV. Energy-driven computing. Phil Trans R Soc A 2020;378(2164):20190158.
[31] Li X, Tang H, Hu G, Zhao B, Liang J. ViPSN-Pluck: a transient-motion-powered motion detector. IEEE Internet Things J 2021;9(5):3372–82.
[32] Fu H, Yeatman EM. Rotational energy harvesting using bi-stability and frequency up-conversion for low-power sensing applications: Theoretical modelling and experimental validation. Mech Syst Signal Process 2019;125:229–44.
[33] Yung KW, Landecker PB, Villani DD. An analytic solution for the force between two magnetic dipoles. Magn Electr Sep 1970;9.
[34] Kim P, Seok J. A multi-stable energy harvester: dynamic modeling and bifurcation analysis. J Sound Vib 2014;333(21):5525–47.
[35] Shu YC, Wang WC, Chang YP. Electrically rectified piezoelectric energy harvesting induced by rotary magnetic plucking. Smart Mater Struct 2018;27(12):125006.
[36] Lo Y, Chen C, Shu Y-C, Lumentut M. Broadband piezoelectric energy harvesting induced by mixed resonant modes under magnetic plucking. Smart Mater Struct 2021;30(10):105026.
[37] Zhang J, Gong S, Li X, Liang J, Wang ZL, Ren K. A wind-driven poly(tetrafluoroethylene) electret and polylactide polymer-based hybrid nanogenerator for self-powered temperature detection system. Adv Sustain Syst 2021;5(1):2000192.
[38] Wang J, Cao Y, Xiang H, Zhang Z, Liang J, Li X, et al. A piezoelectric smart backing ring for high-performance power generation subject to train induced steel-spring fulcrum forces. Energy Convers Manage 2022;257:115442.
[39] Hu G, Zhao C, Yang Y, Li X, Liang J. Triboelectric energy harvesting using an origami-inspired structure. Appl Energy 2022;306:118037.
[40] Liu Q, Li X, Zhang H, Ren J, Yang S, Cao L, et al. IntelliSense silk fibroin ionotronic batteries for wildfire detection and alarm. Nano Energy 2022;101:107630.
[41] Li X, Tang H, Zhu Y, Wang H, Liang J. Power solutions of a vibration-powered sensor node. In: IEEE 9th international power electronics and motion control conference. IEEE; 2020, p. 2513–9.
[42] Li X, Tang H, Hu G, Liang J. Live demo of a transient-motion-powered human motion detector. In: 2021 IEEE international symposium on circuits and systems. 2021, p. 1. http://dx.doi.org/10.1109/ISCAS51556.2021.9401537.